Spectral interference in multiplexed volume Bragg gratings: theoretical calculations and experimental verification

G. B. Ingersoll* and J. R. Leger

Department of Electrical and Computer Engineering, University of Minnesota, 200 Union St. S.E., Minneapolis, Minnesota 55455, USA

*Corresponding author: gbingersoll@gmail.com

Received 4 April 2014; revised 6 July 2014; accepted 13 July 2014; posted 14 July 2014 (Doc. ID 209072); published 18 August 2014

Multiplexed volume Bragg gratings can be applied to many types of broad- and narrowband spectral systems. However, there are often deleterious side effects to combining several gratings into a single holographic optical element, including loss of efficiency in diffracted waves of interest and the introduction of spurious waves. Design of these spectral systems requires analysis methods that are flexible and efficient and that take these side effects into account. We present a matrix-based algorithm for determining diffraction efficiencies of significant coupled waves in these multiplexed grating Holographic optical elements (HOEs). Several carefully constructed experiments with spectrally multiplexed gratings in dichromated gelatin verify our conclusions. © 2014 Optical Society of America

OCIS codes: (090.7330) Volume gratings; (090.6186) Spectral holography; (230.1950) Diffraction gratings; (000.3860) Mathematical methods in physics.

http://dx.doi.org/10.1364/AO.53.005477

1. Introduction

Volume Bragg gratings find uses in a wide range of spectral applications. Holographic optical elements (HOEs) employing these gratings provide high diffraction efficiency and narrowband spectral characteristics to spectral beam combining systems [1–3] and wavelength division multiplexing (WDM) systems [4–6]. Further, volume Bragg gratings can be designed with a broadband characteristic and applied to efficient power generation in spectrum splitting photovoltaic systems [7].

While single volume Bragg gratings are relatively simple to design and construct, there are limitations to the applicability of single grating HOEs in some applications. In beam combining, essentially only two channels can be combined without resorting to a cascade of HOEs. Further, in a broad-spectrum application (e.g., solar spectrum splitting), the approximately sinc-squared nature of the grating's diffraction efficiency as a function of operating wavelength is a poor approximation to an ideal spectral filter. For a single passband, a straightforward dichroic mirror may perform better. In addition, a volume grating, like any diffraction grating, is dispersive, and dispersion over a wide band of interest can complicate the design of the system.

Combining multiple volume gratings in a single element adds design flexibility to these types of narrow- and broadband systems. In a laser beam-combining system, multiplexed volume gratings allow multiple channels to be combined in a single HOE and also provide decoupling between the wavelength of a source and its physical position in the system. This decoupling is not generally available in spectral beam combining systems based on thin gratings, and dichroic filters lead to impractical complex arrangements in systems with many channels. In broadband applications, multiplexing

1559-128X/14/245477-09$15.00/0

gratings have two advantages: (1) the gratings can be tailored to better approximate an ideal spectral filter, and (2) the dispersive effects of the filter can be reduced by overlapping the output spectra of the multiplexed gratings.

Of course, this design flexibility comes at the expense of complexity in the design and analysis of the HOE, and often requires minimization of unwanted cross coupling effects among multiplexed gratings. Efficient mathematical methods are needed to perform this analysis and to optimize systems that utilize multiplexed grating HOEs.

Multiplexed volume Bragg gratings and mathematical methods for their analysis have, indeed, been previously studied for various applications. Many methods find their origins in Kogelnik's coupled wave theory, developed for single volume gratings [8]. Subsequently, Alferness and Case studied cross coupling (i.e., an input wave being coupled to multiple output waves) in two-grating monochromatic systems. Their mathematical methods were based on the so-called thin-grating decomposition [9,10] or involved special cases of monochromatic two-grating systems for which analytical solutions of the coupled wave equations could be found [11].

Other authors also offered solution methods for monochromatic two-grating systems, including multiple-scattering theory [12], vector-synthetic gratings [13], and treatments of double-exposed gratings in both transmission [14] and reflection [15] modes. Minier [16,17] was one of the first to describe spectral interference effects in multiplexed grating systems operating at multiple wavelengths, toward the development of narrowband WDM systems in planar waveguides. That work extended the coupled wave equations to allow both angle and wavelength variation from the Bragg condition, with the resulting equations solved through numerical integration. In addition, Moharam and Gaylord [18] presented their rigorous coupled wave analysis, which eliminates several assumptions present in Kogelnik's and in later work. Namely, the rigorous theory does not neglect boundary diffraction, does not eliminate second-derivatives stemming from the application of the wave equation, and does not assume a single diffracted wave from a grating.

In the current work, an in-depth study of spectral interference in multiplexed volume holograms is conducted, new mathematical methods are derived for calculating the diffraction efficiency of these multiplexed grating systems, and carefully controlled experiments are conducted to verify the theory. The mathematical method presented in Section 2 starts by constructing a characteristic matrix for the grating system, and includes an algorithm to select a set of significant plane-wave diffraction orders to preserve for the analysis. The diffraction efficiencies of the various waves are then computed through straightforward eigenvector decomposition of the matrix. This method is quite flexible for holograms consisting of many gratings, and allows for calculations of direct and cross coupled orders as a function of both incident angle and operating wavelength. The method is also fast, as it relies on efficient matrix manipulation techniques rather than numerical integration. Our overall theory of spectral interference is verified experimentally for a broad-spectrum multiplexed grating pair in Section 3.

2. Multiplexed Grating Algorithm

The mathematical model for quickly calculating diffraction efficiencies in systems of multiplexed volume gratings begins with the well-known model described by Kogelnik [8]. For brevity, many details of Kogelnik's derivation are not included here. However, for clarity, Section 2.A begins with a summary of Kogelnik's symbology and the differential equations describing coupled waves in a single planar volume transmission phase grating. We then convert this model to a matrix formulation before expanding the matrix solution in Section 2.B to treat arbitrary systems of multiplexed plane gratings with plane wave inputs at arbitrary angles and wavelengths.

A. Single Transmission Mode Grating

A single planar volume grating is typically depicted conceptually in a momentum or k-space diagram, as in Fig. 1. Here, the radius of the circle is $\beta = 2\pi n/\lambda$, where n is the bulk index of refraction of the material. Two plane waves are present in the system and are referred to as the reference and signal waves, with field symbols R and S and vector symbols $\boldsymbol{\rho}$ and $\boldsymbol{\sigma}$, respectively. The figure can be interpreted as the condition for grating construction where $\boldsymbol{\rho}$ and $\boldsymbol{\sigma}$ are given and the grating vector $\boldsymbol{K}$ is equal to $\boldsymbol{\rho} - \boldsymbol{\sigma}$. The figure can also be interpreted as the situation for grating reconstruction where $\boldsymbol{\rho}$ and $\boldsymbol{K}$ are given and $\boldsymbol{\sigma}$ is derived. This second interpretation leads to the

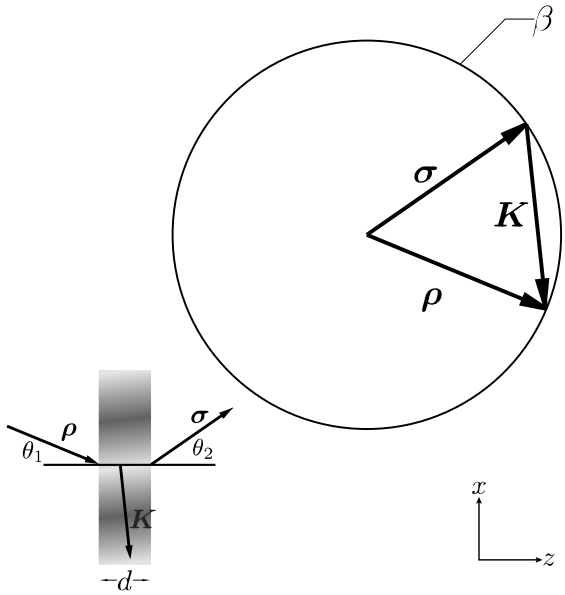

Fig. 1. Momentum or k-space diagram for a single grating. Inset: the physical model of a single grating defining plane wave angles θ_1 and θ_2, and the grating thickness d.

differential equations used to calculate diffraction efficiency for a given input wave.

The electric field in the material is assumed to be the sum of two plane waves, each polarized perpendicular to the plane of incidence:

$$E(x,y,z,t) = R(z)e^{j(\rho\cdot x-\omega t)} + S(z)e^{j(\sigma\cdot x-\omega t)}. \quad (1)$$

At the same time, the grating vector $\boldsymbol{K}$ describes a sinusoidal variation of the index of refraction of the bulk material:

$$\epsilon(x,y,z) = \epsilon_0 + \epsilon_1 \cos \boldsymbol{K}\cdot\boldsymbol{x}, \quad (2)$$

where $\epsilon_0 = n^2$.

Combining these equations with the familiar scalar wave equation, and dropping second derivatives in z, Kogelnik's assumption that "energy interchange between S and R is slow," leads to the system of first-order differential equations:

$$c_R R' = j\kappa S, \quad (3a)$$

$$c_S S' - j\vartheta S = j\kappa R. \quad (3b)$$

Here, primes indicate first derivatives in z and $\kappa = \pi n_1/\lambda$ where n_1 is the index modulation of the grating given by

$$n_1 = \frac{\epsilon_1}{2\sqrt{\epsilon_0}}. \quad (4)$$

In addition, c_R and c_S are the respective direction cosines of the two significant waves

$$c_R = \cos\theta_1 = \frac{\rho_z}{\beta}, \quad (5a)$$

$$c_S = \cos\theta_1 - \frac{|\boldsymbol{K}|}{\beta}\cos\phi = \frac{\sigma_z}{\beta}, \quad (5b)$$

where ϕ is the tilt of the grating relative to the z-axis. Finally, ϑ is the dephasing parameter, defined as

$$\vartheta = \frac{\beta^2-\sigma^2}{2\beta} = |\boldsymbol{K}|\cos(\phi-\theta) - \frac{|\boldsymbol{K}|^2}{4\pi n}\lambda. \quad (6)$$

By assuming solutions of the form $R(z) = ae^{\gamma z}$, with a constant, the system of differential equations can be written in matrix form as

$$\boldsymbol{M}\boldsymbol{x} = \gamma\boldsymbol{x}, \quad (7)$$

where

$$\boldsymbol{M} = \begin{bmatrix} 0 & \frac{j\kappa}{c_R} \\ \frac{j\kappa}{c_S} & \frac{j\vartheta}{c_S} \end{bmatrix}, \quad (8a)$$

$$\boldsymbol{x} = \begin{bmatrix} R \\ S \end{bmatrix}. \quad (8b)$$

For the eigenvectors of $\boldsymbol{M}$ to form an orthonormal basis, $\boldsymbol{M}$ must be symmetric [19]. We can achieve this criterion without loss of generality through a simple variable substitution, where we define

$$\tilde{\boldsymbol{x}} \equiv \begin{bmatrix} \tilde{R} \\ \tilde{S} \end{bmatrix} \equiv \begin{bmatrix} c_R & 0 \\ 0 & \sqrt{c_R c_S} \end{bmatrix}\boldsymbol{x}. \quad (9)$$

Use of variable substitution results in the symmetric matrix

$$\tilde{\boldsymbol{M}} = \begin{bmatrix} 0 & \frac{j\kappa}{\sqrt{c_R c_S}} \\ \frac{j\kappa}{\sqrt{c_R c_S}} & \frac{j\vartheta}{c_S} \end{bmatrix}. \quad (10)$$

The eigenvalues of $\tilde{\boldsymbol{M}}$ are found in the usual fashion by solving

$$\begin{vmatrix} \gamma & \frac{-j\kappa}{\sqrt{c_R c_S}} \\ \frac{-j\kappa}{\sqrt{c_R c_S}} & \gamma - \frac{j\vartheta}{c_S} \end{vmatrix} = 0, \quad (11)$$

which gives

$$\gamma_\pm = \frac{j}{2}\left(\frac{\vartheta}{c_S} \pm \sqrt{\frac{\vartheta^2}{c_S^2} + \frac{4\kappa^2}{c_R c_S}}\right). \quad (12)$$

Defining $\boldsymbol{\xi}_+$ and $\boldsymbol{\xi}_-$ as the (column) eigenvectors of $\tilde{\boldsymbol{M}}$ corresponding to γ_+ and γ_-, respectively, we can use the eigenvalues and the matrices representing the variable substitution to define the transfer matrix of a grating of thickness d as

$$\boldsymbol{G} = \begin{bmatrix} \frac{1}{c_R} & 0 \\ 0 & \frac{1}{\sqrt{c_R c_S}} \end{bmatrix}[\boldsymbol{\xi}_+ \ \boldsymbol{\xi}_-]\begin{bmatrix} e^{\gamma_+ d} & 0 \\ 0 & e^{\gamma_- d} \end{bmatrix}[\boldsymbol{\xi}_+ \ \boldsymbol{\xi}_-]^T\begin{bmatrix} c_R & 0 \\ 0 & \sqrt{c_R c_S} \end{bmatrix}, \quad (13)$$

such that the amplitudes of the R and S waves at the input ($z = 0$) and output ($z = d$) of the grating are related by

$$\boldsymbol{x}_d = \boldsymbol{G}\boldsymbol{x}_0. \quad (14)$$

The boundary conditions for a transmission grating are such that the amplitude of the R wave at $z = 0$ is 1 and the amplitude of the S wave at $z = 0$ is 0. Given these values for the components of $\boldsymbol{x}_0$, the diffraction efficiency of the grating is given by

$$\eta = \frac{c_S}{c_R} S_d S_d^*, \quad (15)$$

where S_d is the S-element of $\boldsymbol{x}_d$. This matches Kogelnik's result for a transmission phase grating.

B. Multiplexed Gratings

The value of converting Kogelnik's single grating method to an explicit matrix solution becomes clear when one must deal with multiple simultaneous gratings under variations in the incident angle and wavelength of the reference wave. Formulating the solution in this way allows a rather straightforward algorithm to determine the N significant waves present in the compound hologram and to build the $N \times N$ characteristic matrix $\boldsymbol{M}$.

A typical situation involving two multiplexed gratings is shown in Fig. 2. Here, the gratings ($\boldsymbol{K}_1$ and $\boldsymbol{K}_2$) share one of their defining angles—note the common direction of $\boldsymbol{\rho}_1$ and $\boldsymbol{\rho}_2$—and have different defining wavelengths, denoted by β_1 and β_2. This system could define, for example, a spectrum splitter or a spectral beam combiner.

When this pair of gratings is reconstructed by a plane wave $\boldsymbol{\rho} = \boldsymbol{\rho}_1$, the momentum diagram appears as in Fig. 3. Here, there are two directly coupled waves: $\boldsymbol{\sigma}_1 = \boldsymbol{\rho} - \boldsymbol{K}_1$ and $\boldsymbol{\sigma}_2 = \boldsymbol{\rho} - \boldsymbol{K}_2$. The input wave is Bragg-matched with $\boldsymbol{K}_1$—the corresponding output vector terminates on the momentum circle—and the input wave is nearly Bragg-matched with $\boldsymbol{K}_2$. Note that, because this situation involves different defining wavelengths for the multiplexed gratings, an input wave cannot, in general, be Bragg-matched with all of the gratings simultaneously. This condition precludes the simplifications that led to an analytical solution for Case's two-grating monochromatic system [11].

In addition to the two directly coupled waves, Fig. 3 also depicts a wave that derives from interaction with both gratings ($\boldsymbol{\sigma}_3 = \boldsymbol{\sigma}_1 - \boldsymbol{K}_2 = \boldsymbol{\rho} - \boldsymbol{K}_1 - \boldsymbol{K}_2$). This cross coupled wave must be included in the mathematical model to achieve accurate results. (This concept was detailed for monochromatic systems in [10]).

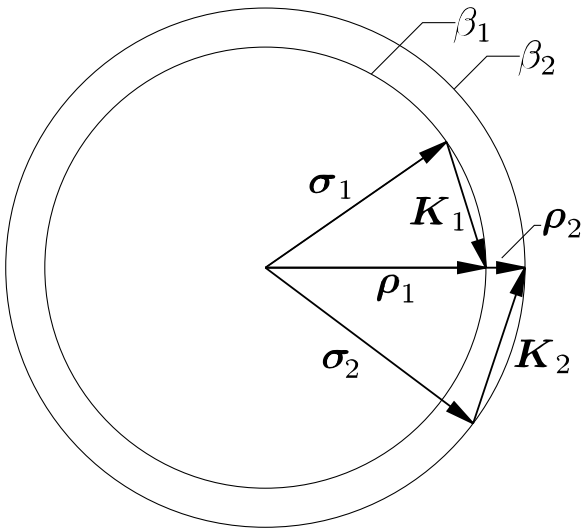

Fig. 2. k-space diagram for defining two multiplexed gratings. These gratings share one of their defining angles and have different central operating wavelengths.

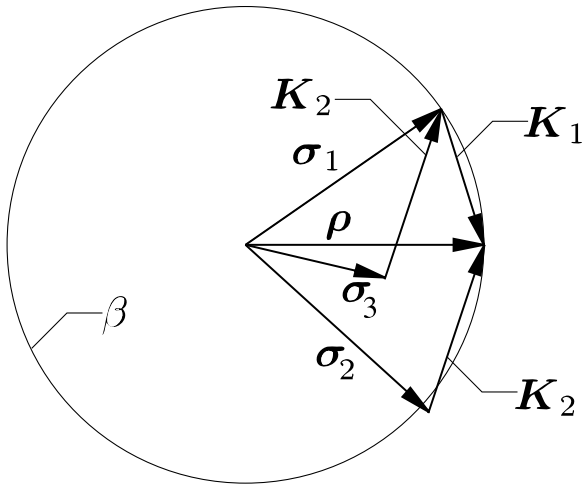

Fig. 3. k-space diagram for reconstructing two multiplexed gratings. From the diagram, waves associated with $\boldsymbol{\sigma}_1$ and $\boldsymbol{\sigma}_2$ are qualitatively expected to be significant to the solution. However, $\boldsymbol{\sigma}_3$ is not qualitatively expected to be significant because $|\boldsymbol{\sigma}_3|$ differs so greatly from β.

The algorithm for building the characteristic matrix for a multiplexed system then proceeds as follows. Given the input wavevector and the grating vectors, all combinations of directly coupled waves ($\boldsymbol{\sigma}_j = \boldsymbol{\rho} \pm \boldsymbol{K}_i$) are constructed. Some of these vector combinations will turn out to be insignificant to the diffraction efficiency calculation especially when their wave vectors terminate far from the momentum circle. (This can be seen qualitatively for $\boldsymbol{\sigma}_3$ in Fig. 3). This is equivalent to a wave having a large dephasing parameter [see Eq. (6)], so the dephasing parameter is used in the algorithm as a measure for eliminating waves from consideration.

Those waves with dephasing parameters exceeding some limit are eliminated, and then cross coupled waves are determined through vector combination of the directly coupled wavevectors and the grating vectors. Again, insignificant waves are eliminated. This process continues through a pre-determined number of diffraction stages, or until a diffraction stage results in no new significant waves.

An appropriate limit for the dephasing parameter is dependent on the exact nature of the system being modeled and must be determined iteratively. If the limit is set too low, then waves with significant energy could be eliminated from the model, leading to inaccurate results and poor system optimization. Conversely, if the limit is set too high, then the size of the characteristic matrix of the system increases unnecessarily, leading to longer execution times for the calculations, with no significant difference in the end result.

One technique for determining the dephasing limit for a given system is to set a relatively high limit and then calculate diffraction efficiencies of the significant waves for a sparse collection of input wavelengths. If the diffraction efficiency of any included waves in the domain of interest does not exceed some small value (e.g., 0.1%), then the dephasing limit can

be reduced to eliminate these waves from the model; thereby, the diffraction efficiencies of the significant waves can be more quickly calculated for a dense set of inputs.

When all significant waves are determined, the characteristic matrix $\tilde{\boldsymbol{M}}$ for the system can be constructed directly. Diagonal elements consist of functions of the respective waves' dephasing parameters. ϑ corresponding to the reference wave $\boldsymbol{\rho}$ is, by definition, zero, thus, $\tilde{M}_{00} = 0$. Other diagonal elements follow:

$$\tilde{M}_{mm} = \frac{j\vartheta_m}{c_{Sm}}, \qquad m \neq 0. \tag{16}$$

Conceptually, off-diagonal elements link waves to each other through gratings. These elements are functions of the two waves' direction cosines and of the grating's coupling coefficient κ. If wave m and wave n are coupled through grating p, then the corresponding (symmetric) matrix elements become

$$\tilde{M}_{mn} = \tilde{M}_{nm} = \frac{j\kappa_p}{\sqrt{c_{Sm}c_{Sn}}}, \qquad m \neq n. \tag{17}$$

For example, referencing Fig. 3, Grating 2 couples wave S_1 (corresponding to $\boldsymbol{\sigma}_1$) to wave S_3, so the corresponding matrix elements are

$$\tilde{M}_{13} = \tilde{M}_{31} = \frac{j\kappa_2}{\sqrt{c_{S1}c_{S3}}}. \tag{18}$$

Likewise, Grating 1 couples the reference wave to wave S_1, leading to off-diagonal elements

$$\tilde{M}_{01} = \tilde{M}_{10} = \frac{j\kappa_1}{\sqrt{c_R c_{S1}}}. \tag{19}$$

All other matrix elements are 0, so for the system depicted in Fig. 3, assuming ϑ_3 is quantitatively small enough such that wave S_3 is not eliminated, the nonzero elements in the 4×4 characteristic matrix follow:

$$\tilde{\boldsymbol{M}} = \begin{bmatrix} 0 & \cdot & \cdot & 0 \\ \cdot & 0 & 0 & \cdot \\ \cdot & 0 & \cdot & 0 \\ 0 & \cdot & 0 & \cdot \end{bmatrix}. \tag{20}$$

(Recall that the reference wave is Bragg-matched with grating 1, so $\vartheta_1 = 0$ and $\tilde{M}_{11} = 0$.)

So far, TE-polarization (i.e., electric field vectors perpendicular to the plane of incidence) has been assumed. However, TM-polarization, or indeed, arbitrary polarization, can be handled in the model at this point with a straightforward addition to the characteristic matrix. Again, following [8], the coupling between the two waves, S_m and S_n is reduced by the dot product of their respective (normalized) polarization vectors $\langle \boldsymbol{s}_m \cdot \boldsymbol{s}_n \rangle$, resulting in a more general form for Eq. (17):

$$\tilde{M}_{mn} = \tilde{M}_{nm} = \frac{j\kappa_p \langle \boldsymbol{s}_m \cdot \boldsymbol{s}_n \rangle}{\sqrt{c_{Sm}c_{Sn}}}, \qquad m \neq n. \tag{21}$$

Once the characteristic matrix has been fully determined, the relative power distribution among all of the significant waves is calculated in a method analogous to the discussion above. Continuing with the example system of Fig. 3, the transfer matrix Eq. (22) is built in an analogous fashion to Eq. (13):

$$G = \begin{bmatrix} \frac{1}{c_R} & 0 & 0 & 0 \\ 0 & \frac{1}{\sqrt{c_R c_{S1}}} & 0 & 0 \\ 0 & 0 & \frac{1}{\sqrt{c_R c_{S2}}} & 0 \\ 0 & 0 & 0 & \frac{1}{\sqrt{c_R c_{S3}}} \end{bmatrix} [\boldsymbol{\xi}_1 \quad \boldsymbol{\xi}_2 \quad \boldsymbol{\xi}_3 \quad \boldsymbol{\xi}_4] \begin{bmatrix} e^{\gamma_1 d} & 0 & 0 & 0 \\ 0 & e^{\gamma_2 d} & 0 & 0 \\ 0 & 0 & e^{\gamma_3 d} & 0 \\ 0 & 0 & 0 & e^{\gamma_4 d} \end{bmatrix}$$
$$\times [\boldsymbol{\xi}_1 \quad \boldsymbol{\xi}_2 \quad \boldsymbol{\xi}_3 \quad \boldsymbol{\xi}_4]^T \begin{bmatrix} c_R & 0 & 0 & 0 \\ 0 & \sqrt{c_R c_{S1}} & 0 & 0 \\ 0 & 0 & \sqrt{c_R c_{S2}} & 0 \\ 0 & 0 & 0 & \sqrt{c_R c_{S3}} \end{bmatrix}, \tag{22}$$

and the individual field amplitudes are found analogously to Eq. (14):

$$\boldsymbol{x}_d = \begin{bmatrix} R_d \\ S_{1d} \\ S_{2d} \\ S_{3d} \end{bmatrix} = \boldsymbol{G} \begin{bmatrix} 1 \\ 0 \\ 0 \\ 0 \end{bmatrix}. \tag{23}$$

Finally, the diffraction efficiencies of the individual waves are found from

$$\eta_i = \frac{c_{Si}}{c_R} S_{id} S_{id}^*. \tag{24}$$

Using optimized libraries of standard matrix operations (e.g., architecture-specific implementations of

BLAS, LAPACK, ATLAS, etc.), these calculations execute quickly even for 10 × 10 and larger matrices. While, again, rigorous coupled wave methods are not used, the approximations employed here allow for this efficient calculation method which, in turn, provides for efficient optimization algorithms for systems of multiplexed volume gratings.

To ensure that these approximations do not preclude accurate results, we verified this mathematical model experimentally, as detailed in the next section.

3. Experimental Verification

To demonstrate the validity of the mathematical model developed in Section 2, we constructed multiplexed gratings in PFG–04 dichromated gelatin. The efficiency of various diffraction orders were then characterized as a function of input wavelength and compared with the model.

A. Grating Design

The exposure source used for the experiment was a Coherent Verdi laser operating at 532 nm and 5 Watts. The beam from this source was split, filtered, expanded, and collimated. Then, each individual beam was redirected to the holographic plate by mirrors mounted on rotation stages. The mirrors were rotated to set each beam's angle relative to the plate. These angles and the laser wavelength completely determine the period and tilt of the resulting gratings.

The steering mirrors in the exposure setup were also allowed to translate along one axis to set the position of the overlap of the two beams on the plate. (Note that the coherence length of this laser is greater than 20 m; therefore, path length-matching of the beams on the scale of the optical tabletop is of little concern.) Translating the mirrors allowed for multiple experiments on a single plate and, more importantly, allowed the two exposures of a particular experiment to only partially overlap. This, in turn, allowed characterization of each grating individually, as well as characterization of the multiplexed pair.

We used the mathematical model to determine period and tilt parameters for a grating pair that would operate over much of the visible spectrum. This pair was also designed to exhibit easily measurable cross coupling over a sufficiently wide wavelength range. Exposure energies—beam intensity, beam balance ratio, and exposure time—were determined iteratively to achieve the desired peak diffraction efficiency, which was deliberately kept low in these experiments.

Data from the literature [20] suggest that the effective dynamic range of PFG–04 dichromated gelatin plates corresponds to an index modulation n_1 of approximately 0.012. To avoid clipping the desired sinusoidal index variation through multiple exposures, relatively low exposure energy was used for these experiments. Staying well within the dynamic range of the material ensured that any diffraction orders evident during hologram reconstruction were a result of grating direct and cross coupling predicted by the mathematical model and not the result of nonlinear effects of the material.

B. Measurement

To reduce the impact of material and exposure inconsistency given our operating regime, the multiplexed gratings were exposed on the holographic plate with only partial overlap. This allowed each grating to be characterized individually. The single gratings' diffraction orders were measured as a function of input angle using a 632 nm laser source. Angle was used as the free variable because the grating period and tilt can be largely determined by finding the two input angles at which there is a diffraction efficiency peak for a fixed wavelength. This cannot be achieved through a variation in wavelength alone.

However, toward the goal of applying multiplexed gratings to spectral applications, we then characterized the multiplexed pair by fixing the input angle and varying the input wavelength. The source in this case consisted of a Bausch and Lomb grating monochromator with a tungsten lamp. Imaging optics were included after the output slit of the monochromator to approximate a plane wave at the holographic grating, and a polarizer was inserted to linearly polarize the light perpendicular to the plane of incidence with the holographic plate. The monochromator's input and output slit widths were set to provide a half-power output bandwidth of 5 nm.

Once each grating of a pair was characterized individually, its modeled parameters were adjusted to match the experimental data. The period and tilt of a grating and the local thickness of the holographic material vary from anticipated values due to gelatin shrinkage during development, and the final index modulation of a given grating is somewhat unpredictable. This experimental variability is effectively eliminated by adjusting the model to match (1) measured values for the peak diffraction efficiency, (2) the two incidence angles at which diffraction efficiency peaks occur at the measurement wavelength, and (3) the input angles corresponding to the first zeros of the diffraction efficiency curve.

After the single grating models' parameters are adjusted to fit experimental data as a function of input angle, the multiplexed model is recalculated for a fixed input angle but variable wavelength. These theoretical curves are then compared with experimental measurements of the multiplexed gratings without further adjustment. Not only is the initial single grating characterization versus input angle more straightforward experimentally, comparing data against both input angle and wavelength variation further reinforces the validity of the mathematical model.

C. Results

The experimental results for two different grating pair designs are given in the following sections. The first pair exhibits cross coupling interference.

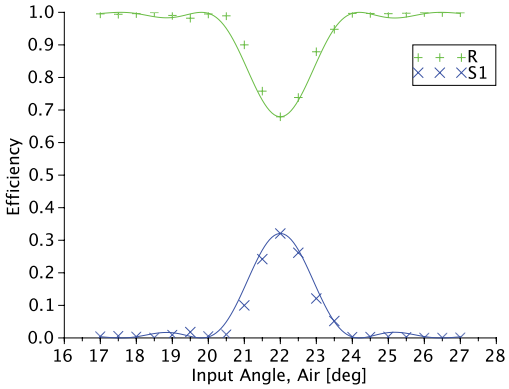

Fig. 4. Diffraction efficiency of Grating 1 as a function of input angle for an input wavelength of 632.8 nm. Solid lines show the theoretical efficiency after adjusting the model to fit the measured data.

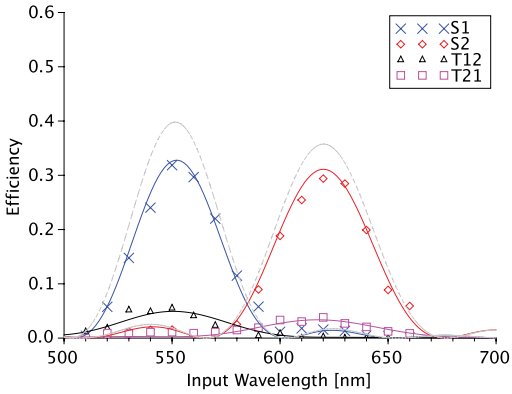

Fig. 5. Diffraction efficiency of the significant output waves of the interfering grating pair as a function of input wavelength for an input angle (in air) of 18.5°. Measured data is superimposed on theoretical data. The lighter dashed curves indicate what the S-wave diffraction efficiency of each grating would be if the other grating was not present in the holographic element.

The second pair is similar, but Grating 2's construction angles were adjusted to eliminate the interference. This second pair is used as a control to ensure all of the gratings are operating in a linear region of the material.

1. *Interfering Gratings*

Characterizing the individual gratings of the interfering pair and feeding this data back into the model resulted in Fig. 4, which plots diffraction efficiency versus input angle for Grating 1 and a similar plot (not shown) for Grating 2. The solid curve represents the adjusted model, and the measured data points are superimposed. An expanded and collimated beam from a 632.8 nm He–Ne laser was the light source. The gratings' defining parameters determined from the data fit are given in Table 1.

When the interfering multiplexed pair is characterized as a function of input wavelength, the diffraction efficiency curves appear, as shown in Fig. 5. The solid curves are theoretical data from the model, with measured data points for each diffracted wave superimposed. The lighter dashed curves show what the S-wave diffraction efficiency of each grating would be if the other grating were not present.

Note that the experimental data matches quite well with the theory. There is a significant decrease in peak diffraction efficiency for each grating, and the two cross coupled waves appear as expected. The cross coupled waves are given unique symbols, T_{12} and T_{21}, corresponding to vectors $\boldsymbol{\tau}_{12} = \boldsymbol{\rho} - \boldsymbol{K}_1 + \boldsymbol{K}_2$ and $\boldsymbol{\tau}_{21} = \boldsymbol{\rho} + \boldsymbol{K}_1 - \boldsymbol{K}_2$, respectively.

2. *NonInterfering Gratings*

To further reinforce that the above results are due to the physics of a multiplexed grating pair and not the result of nonlinear material effects, a second, similar grating pair was constructed. This second pair was modified from the first to eliminate the occurrence of cross coupled waves while keeping similar modulation levels for each grating. Specifically, the operating angles of the second grating were modified to detune the cross coupling with the first grating.

Again, the individual gratings were characterized as a function of input angle at a fixed wavelength, and the model parameters were adjusted to fit the experimental data. The resulting grating parameters for the noninterfering pair are given in Table 2. Note that the gratings' index modulation values in this case are actually slightly higher than for the interfering grating pair discussed above.

Plotting the adjusted model as a function of input wavelength results in the solid curves of Fig. 6 and, again, experimental measurements are superimposed. Note that, as in Fig. 5, the gratings' nonmultiplexed efficiency curves are included, but cannot be seen in the plot because they lie directly behind the multiplexed efficiency curves. That is, there is no significant expected change in S-wave diffraction efficiency, and no appearance of T-wave (cross coupled) efficiency resulting from multiplexing this grating pair for this wavelength range and input angle. Also

Table 1. Parameters of Interfering Grating Pair as Determined by Fitting Measured Diffraction Efficiency Data to the Theoretical Model

	Grating 1	Grating 2
Bragg angle 1 [deg., air at 632.8 nm]	22.00	18.92
Bragg angle 2 [deg., air at 632.8 nm]	−31.17	−31.17
Period [μm]	0.71	0.75
Index modulation n_1	0.0040	0.0040
Thickness d [μm]	29.0	29.0

Table 2. Parameters of NonInterfering Grating Pair Determined by Fitting Measured Diffraction Efficiency Data to the Theoretical Model

	Grating 1	Grating 2
Bragg angle 1 [deg., air at 632.8 nm]	22.00	18.92
Bragg angle 2 [deg., air at 632.8 nm]	−31.17	−39.50
Period [μm]	0.71	0.66
Index Modulation n_1	0.0043	0.0046
Thickness d [μm]	29.0	29.0

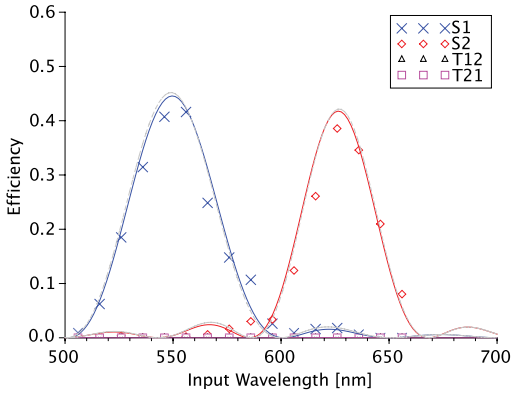

Fig. 6. Diffraction efficiency of the significant output waves of the noninterfering grating pair as a function of input wavelength for an input angle (in air) of 18.5°. Measured data is superimposed on theoretical data.

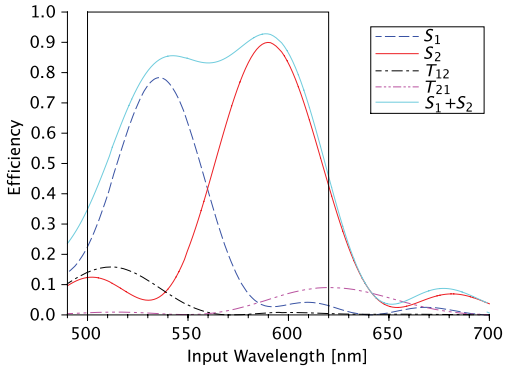

Fig. 7. Diffraction efficiencies versus wavelength of various diffraction orders for an example multiplexed transmission grating pair compared with an ideal bandpass response. Note how the combination of the two directly coupled waves (S_1 and S_2) approaches the ideal response, but multiplexing the gratings also gives rise to stray light in the system in the form of cross coupled waves T_{12} and T_{21}.

note the good fit of the experimental data reinforcing that nonlinear material effects are not at play here.

4. Discussion

The mathematical method presented here is applicable to both broad- and narrowband systems, where maximizing efficiency is a design goal. A holographic spectrum splitter is a fitting broadband system, whereas a spectral beam combiner is a representative narrowband system.

A. Holographic Spectrum Splitter

Improving the efficiency of photovoltaic (PV) power generation systems is an important contemporary topic for optical engineers and physicists. Spectrum splitting systems [21] improve solar conversion efficiency by employing multiple, diverse PV cells optimized for different portions of the solar spectrum and, therefore, require efficient means of redirecting appropriate spectral bands onto the corresponding cells.

In an ideal system employing two bandgaps, the spectrum splitting filter would have infinitely steep transitions, diffracting all of the photons above some cutoff energy and allowing the remaining photons to pass through unaffected. A single volume Bragg grating, with its approximately sinc-squared diffraction efficiency versus wavelength characteristic, does a qualitatively poor job of approximating this desired rectangular filter over a wide band of interest. In addition, employing a single grating over a wide band will result in significant dispersion in the diffracted light, which can complicate the design of such a system.

Employing multiplexed gratings in a spectrum splitting filter can alleviate both of these issues. By optimizing the characteristics of two gratings working together, the diffraction efficiency of the HOE over the band of interest can approach the rectangular ideal and improving the conversion efficiency of the system. Moreover, because each grating is effective over only roughly half of the band of interest, the overall dispersion of the HOE can be reduced, potentially simplifying the overall system at the expense of a more complicated grating structure. However, multiplexing gratings also give rise to additional cross coupled waves, which should be minimized. An example theoretical response for two multiplexed gratings is shown in Fig. 7.

To engineer and optimize such systems, an efficient method for calculating diffraction efficiency of both desired and spurious coupled waves in multiplexed gratings is needed. We can employ the method presented in the preceding sections in an optimization algorithm that tailors two or more multiplexed gratings to (1) maximize diffraction efficiency in-band, (2) minimize diffraction efficiency out-of-band (i.e., side-lobes), (3) minimize grating cross coupling and spurious coupled waves (i.e., stray light), and (4) minimize overall dispersion. Because our method relies only on straightforward vector arithmetic and well-optimized matrix operations, these calculations have been sufficiently fast for use in our work to-date with particle swarm optimization techniques.

B. Spectral Beam Combiner

The basic goal of a spectral beam-combining system is to incoherently combine multiple laser sources at different wavelengths into a single high-power output. This output power increase comes at the expense of increased output bandwidth, so often minimizing output bandwidth or, equivalently, maximizing channel density is a secondary goal.

In contrast to, for example, a simple blazed grating, the ability to decouple the physical position of a source from its wavelength can be advantageous to the mechanical design of such a system, and employing multiplexed volume gratings allows for this flexibility. Of course, with this flexibility comes the cost of analyzing and optimizing these HOEs to avoid the adverse effects of grating interference and cross coupled waves, which result in a decrease in the overall combining efficiency of the system.

Previous related work from the literature for WDM systems often simply suggests increasing the channel spacing to 1.5 [22], or three times [23] or more the individual channel width so that the gratings operate essentially independently. This simplifies the analysis in many ways, but also could unnecessarily increase the overall bandwidth of the system, depending on competing requirements. If a narrow operating bandwidth is a goal, as well as high-efficiency, the techniques presented here can be used to optimize such a system in the presence of grating interference effects. In particular, an optimization algorithm can position sources in space (i.e., set their angles of incidence) and spectrum (i.e., set the center wavelengths of the channels) and also prescribe the material thickness (which has a strong effect on channel width) to maximize channel density and overall combining efficiency.

5. Conclusion

Broadband spectral systems employing multiplexed volume Bragg gratings must be carefully analyzed to understand and avoid grating interference effects that reduce peak diffraction efficiency and introduce undesirable spurious diffraction orders. Here, we have introduced a straightforward matrix method for calculating diffraction efficiency in multi-grating systems that accounts for diffraction orders of interest as well as spurious orders.

Although the method is also suitable for analyzing diffraction efficiency as a function the angle of incidence of the system, our focus here has been on variations of the input wavelength. Our experimental data with broadband two-grating holographic elements confirms the theory, and this method can now be applied to optimization algorithms for laser beam-combining, spectral splitting, and other spectral systems utilizing multiplexed volume Bragg gratings.

References

1. I. V. Ciapurin, L. B. Glebov, L. N. Glebova, V. I. Smirnov, and E. V. Rotari, "Incoherent combining of 100 W Yb–fiber laser beams by PTR Bragg grating," Proc. SPIE **4974**, 209–219 (2003).
2. B. Chann, A. K. Goyal, T. Y. Fan, A. Sanchez-Rubio, B. L. Volodin, and V. S. Ban, "Efficient, high-brightness wavelength-beam-combined commercial off-the-shelf diode stacks achieved by use of a wavelength-chirped volume Bragg grating," Opt. Lett. **31**, 1253–1255 (2006).
3. A. Sevian, O. Andrusyak, I. V. Ciapurin, V. I. Smirnov, G. B. Venus, and L. B. Glebov, "Efficient power scaling of laser radiation by spectral beam combining," Opt. Lett. **33**, 384–386 (2008).
4. P. Boffi, M. C. Ubaldi, D. Piccinin, C. Frascolla, and M. Martinelli, "1550 nm volume holography for optical communication devices," IEEE Photon. Technol. Lett. **12**, 1355–1357 (2000).
5. S. F. Chen, C. S. Wu, and C. C. Sun, "Design for a high dense wavelength division multiplexer based on volume holographic gratings," Opt. Eng. **43**, 2028–2033 (2004).
6. S. Datta and S. R. Forrest, "Low through-channel loss wavelength multiplexer using multiple transmission volume Bragg gratings," J. Opt. Soc. Am. A **22**, 1624–1629 (2005).
7. D. Lin, E. Torrey, J. Leger, and P. Cohen, "Lossless holographic spectrum splitter in lateral photovoltaic devices," in *37th IEEE Photovoltaic Specialists Conference* (IEEE, 2011), pp. 894–898.
8. H. Kogelnik, "Coupled wave theory for thick hologram gratings," Bell Syst. Tech. J. **48**, 2909–2947 (1969).
9. R. Alferness, "Analysis of optical propagation in thick holographic gratings," Appl. Phys. **7**, 29–33 (1975).
10. R. Alferness and S. K. Case, "Coupling in doubly exposed, thick holographic gratings," J. Opt. Soc. Am. **65**, 730–739 (1975).
11. S. K. Case, "Coupled wave theory for multiply exposed thick holographic gratings," J. Opt. Soc. Am. **65**, 724–729 (1975).
12. K. Tu, T. Tamir, and H. Lee, "Multiple-scattering theory of wave diffraction by superposed volume gratings," J. Opt. Soc. Am. A **7**, 1421–1435 (1990).
13. J. H. Zhao, X. N. Shen, and X. Y. Xia, "Beam splitting, combining, and cross coupling through multiple superimposed volume-index gratings," Opt. Laser Technol. **33**, 23–28 (2001).
14. R. Kowarschik, "Diffraction efficiency of sequentially stored gratings in transmission volume holograms," Opt. Acta **25**, 67–81 (1978).
15. R. Kowarschik, "Diffraction efficiency of sequentially stored gratings in reflection volume holograms," Opt. Quantum Electron. **10**, 171–178 (1978).
16. V. Minier, A. Kevorkian, and J. M. Xu, "Superimposed phase gratings in planar optical waveguides for demultiplexing applications," IEEE Photon. Technol. Lett. **5**, 330–333 (1993).
17. V. Minier and J. M. Xu, "Coupled-mode analysis of superimposed phase grating guided-wave structures and integrating coupling effects," Opt. Eng. **32**, 2054–2063 (1993).
18. M. G. Moharam and T. K. Gaylord, "Rigorous coupled wave analysis of planar-grating diffraction," J. Opt. Soc. Am. **71**, 811–818 (1981).
19. T. Rowland, "Orthonormal basis," 2014, http://mathworld.wolfram.com/OrthonormalBasis.html.
20. A. Villamarin, J. Atencia, M. V. Collados, and M. Quintanilla, "Characterization of transmission volume holographic gratings recorded in Slavich PFG04 dichromated gelatin plates," Appl. Opt. **48**, 4348–4353 (2009).
21. A. Barnett, "Very high efficiency solar cell modules," Prog. Photovoltaics **17**, 75–83 (2009).
22. A. Othonos, J. Bismuth, M. Sweeny, A. Kevorkian, and J. M. Xu, "Superimposed grating wavelength division multiplexing in Ge-doped SiO2/Si planar waveguides," Opt. Eng. **37**, 717–720 (1998).
23. X. Fu, M. Fay, and T. M. Xu, "18 supergrating wavelength-division demultiplexer in a silica planar waveguide," Opt. Lett. **22**, 1627–1629 (1997).